Title

Structural and practical identifiability of contrast transport models for DCE-MRI

Permalink

https://escholarship.org/uc/item/2k68709d

Journal

PLOS Computational Biology, 20(5)

ISSN

1553-734X

Authors

Conte, Martina

Woodall, Ryan T

Gutova, Margarita

et al.

Publication Date

2024

DOI

10.1371/journal.pcbi.1012106

Peer reviewed

Structural and practical identifiability of contrast transport models for DCE-MRI

Martina Conte[1,2]*, **Ryan T. Woodall**[2], **Margarita Gutova**[3], **Bihong T. Chen**[4], **Mark S. Shiroishi**[5], **Christine E. Brown**[6], **Jennifer M. Munson**[7], **Russell C. Rockne**[2]*

1 Department of Mathematical Sciences "G. L. Lagrange", Politecnico di Torino, Torino, Italy, 2 Division of Mathematical Oncology and Computational Systems Biology, Department of Computational and Quantitative Medicine, Beckman Research Institute, City of Hope National Medical Center, Duarte, California, United States of America, 3 Department of Stem Cell Biology and Regenerative Medicine, Beckman Research Institute, City of Hope National Medical Center, Duarte, California, United States of America, 4 Department of Diagnostic Radiology, City of Hope National Medical Center, Duarte, California, United States of America, 5 Department of Radiology, Keck School of Medicine of the University of Southern California, Los Angeles, California, United States of America, 6 Departments of Hematology & Hematopoietic Cell Transplantation and Immuno-Oncology, Beckman Research Institute, City of Hope National Medical Center Duarte, California, United States of America, 7 Fralin Biomedical Research Institute, Virginia Tech, Roanoke, Virginia, United States of America

* mconte@coh.org (MC); rrockne@coh.org (RCR)

Abstract

Contrast transport models are widely used to quantify blood flow and transport in dynamic contrast-enhanced magnetic resonance imaging. These models analyze the time course of the contrast agent concentration, providing diagnostic and prognostic value for many biological systems. Thus, ensuring accuracy and repeatability of the model parameter estimation is a fundamental concern. In this work, we analyze the structural and practical identifiability of a class of nested compartment models pervasively used in analysis of MRI data. We combine artificial and real data to study the role of noise in model parameter estimation. We observe that although all the models are structurally identifiable, practical identifiability strongly depends on the data characteristics. We analyze the impact of increasing data noise on parameter identifiability and show how the latter can be recovered with increased data quality. To complete the analysis, we show that the results do not depend on specific tissue characteristics or the type of enhancement patterns of contrast agent signal.

Author summary

In the last decades, study and quantification of tissue perfusion parameters related to blood flow and transport have acquired a significant importance in the analysis of dynamic contrast-enhanced magnetic resonance imaging (DCE-MRI). In fact, concentration time course data derived from DCE-MRI are essential elements for many computational biological applications, ranging from tumor grading assessment to prediction of antiangiogenic treatment response. Contrast agent transport models have been developed and widely used for the analysis of this data, providing diagnostic and prognostic value. Thus, there is a need to ensure reliability and reproducibility of the transport model

parameter estimations. Here we propose the analysis of structural and practical model identifiability, combining artificial and real data to study the role of noise in parameter estimation. The results provide a mathematical explanation for the lack of repeatability of DCE-MRI quantification as well as emphasize the need for new DCE-MRI acquisition protocols standards and quantification methods.

1 Introduction

Contrast agent transport models have been developed and used for decades in the analysis of concentration time course data derived from dynamic contrast-enhanced magnetic resonance imaging (DCE-MRI), and they are essential elements of many computational clinical applications [1–9]. DCE-MRI transport models are based on linear ordinary differential equations with compartments describing the concentration of the contrast agent (CA) in tissue and vasculature. These models assume the compartments are well-mixed, i.e., contrast agent distributes evenly throughout the compartment instantaneously, such that contrast concentration is only a function of time, and not space, within an individual voxel. Several models have been formulated [10] based on different assumptions and simplifications to describe the blood–tissue exchanges of the administered contrast agent between compartments. The kinetic parameters derived from these models have been applied to a wide range of biological settings, including cancer, and have provided compelling diagnostic and prognostic value [11] as well as detecting early response to treatment [12].

Here we consider the structural and practical identifiability of four nested contrast transport compartmental models frequently used to analyze DCE-MRI data. Identifiability is a fundamental property to create models able to capture the dynamics shown in the data with well-determined parameters [13, 14]. The issue of model identifiability revolves around the question of whether it is possible to use data to accurately and uniquely estimate parameters in the model. Generally, the larger the number of compartments in a model, the higher the accuracy, but at the cost of higher analysis complexity. Moreover, the more parameters are included, the higher the probability of having a non-unique combination of model parameters that can accurately characterize the dynamics, underpinning the concept of structural identifiability. Therefore, there is a need to investigate how the kinetic parameters involved in the class of nested models used in DCE-MRI analysis can be determined, and what affects their identifiability, even in simple cases. Model identifiability becomes especially important for biological systems due to the limited availability and quality of the data [15–17]. Moreover, the amount and the quality of the data have a strong impact on the identifiability of some parameters and, thus, on model outcomes and predictions.

Structural identifiability determines if the model structure is well-defined, however it is not sufficient to ensure the robustness of model outcomes when dealing with experimental biological data to inform the model. In fact, it does not guarantee successful parameter estimation when, for instance, there is a limited amount or a quality of the experimental data, with large measurement noise. This is where the study of practical identifiability takes importance and a careful analysis of both types of identifiability becomes vital. In this work, we analyze the entire family of nested contrast transport models from both structural and practical viewpoints. To the best of our knowledge, few works in the literature have analyzed both structural and practical identifiability aspects of transport models used for DCE-MRI data, mainly focusing on the practical identifiability and only for a subset of these models [18–23].

This work is organized as follows. In Section 2, we describe the theoretical aspects of structural and practical identifiability, DCE-MRI data, and the class of considered models. Next, in Section 3, we provide structural and practical identifiability analysis of the most complex member of the family of models, the Leaky Tofts–Kety model, applied to glioblastoma brain cancer data. We comment on the outcomes and implications in Section 4. Finally, in S1–S3 Text, we provide results concerning the nested family of sub-models as well as additional breast cancer data.

2 Materials and methods

2.1 Ethics statement

The study of publicly available data and retrospective analysis of City of Hope patient data were approved with a waiver of consent by the City of Hope Institutional Review Board, Protocol 15286.

2.2 Theory of nested DCE-MRI transport models

Compartmental models of contrast transport for DCE-MRI are constructed assuming that the total tissue CA concentration $C_t(t)$ can be modeled as the sum of the CA concentration in the plasma space (PS) ($C_p(t)$) and in the extracellular extravascular space (EES) ($C_e(t)$), i.e.

$$C_t(t) = v_p C_p(t) + v_e C_p(t) \tag{1}$$

where v_e and v_p are the fractional EES and plasma volumes, respectively. The explicit description of the CA concentration in each of these compartments depends on the assumptions made to estimate both $C_e(t)$ and $C_p(t)$ and, thus, on the chosen model, as illustrated in Fig 1A.

The CA concentration for the plasma compartment, $C_p(t)$, is assumed to be not affected by local transport and it is given by the empirical vascular input function (VIF):

$$C_p(t) = VIF(t). \tag{2}$$

The dynamics of the VIF are characterized by a sharp uptake, followed by a peak value, and then a washout dynamic (Fig 1B). Several techniques have been proposed to measure the VIF [10, 24]. Here we consider two different estimation methods. First, we consider a population-based analytical expression of the VIF, commonly referred to as the Parker VIF [25], and second we estimate the VIF directly from the MRI signal [26]. The Parker VIF uses a mixture of 2 Gaussians plus an exponential modulated by a sigmoid function:

$$VIF(t) = \sum_{n=1}^{2} \frac{A_n}{\sigma_n \sqrt{2\pi}} \exp\left(-(t - T_n)^2 / 2\sigma_n^2\right) + \frac{\alpha \exp(-\beta t)}{1 + \exp(-l(t - \tau))} \tag{3}$$

Here A_n, T_n, and σ_n are the scaling constants, centers, and widths of the nth Gaussian, α and β are the amplitude and decay constant of the exponential, and l and τ are the width and center of the sigmoid, respectively. For the second method, VIF estimation is performed by drawing a region of interest (ROI) on a major vessel in the tissue and directly quantifying the contrast agent concentration, assuming the CA bolus arrives simultaneously to the entire tissue of interest. Population-based VIFs are widely used in DCE-MRI due to their simplicity and the fact that they do not require additional measurements, though they may ignore inter-subject variability. In contrast, the accuracy of individual-based VIFs derived from estimations of the CA concentration in large vessels depends on MRI characteristics, which may contribute to identifiability issues, as will become apparent through our analysis.
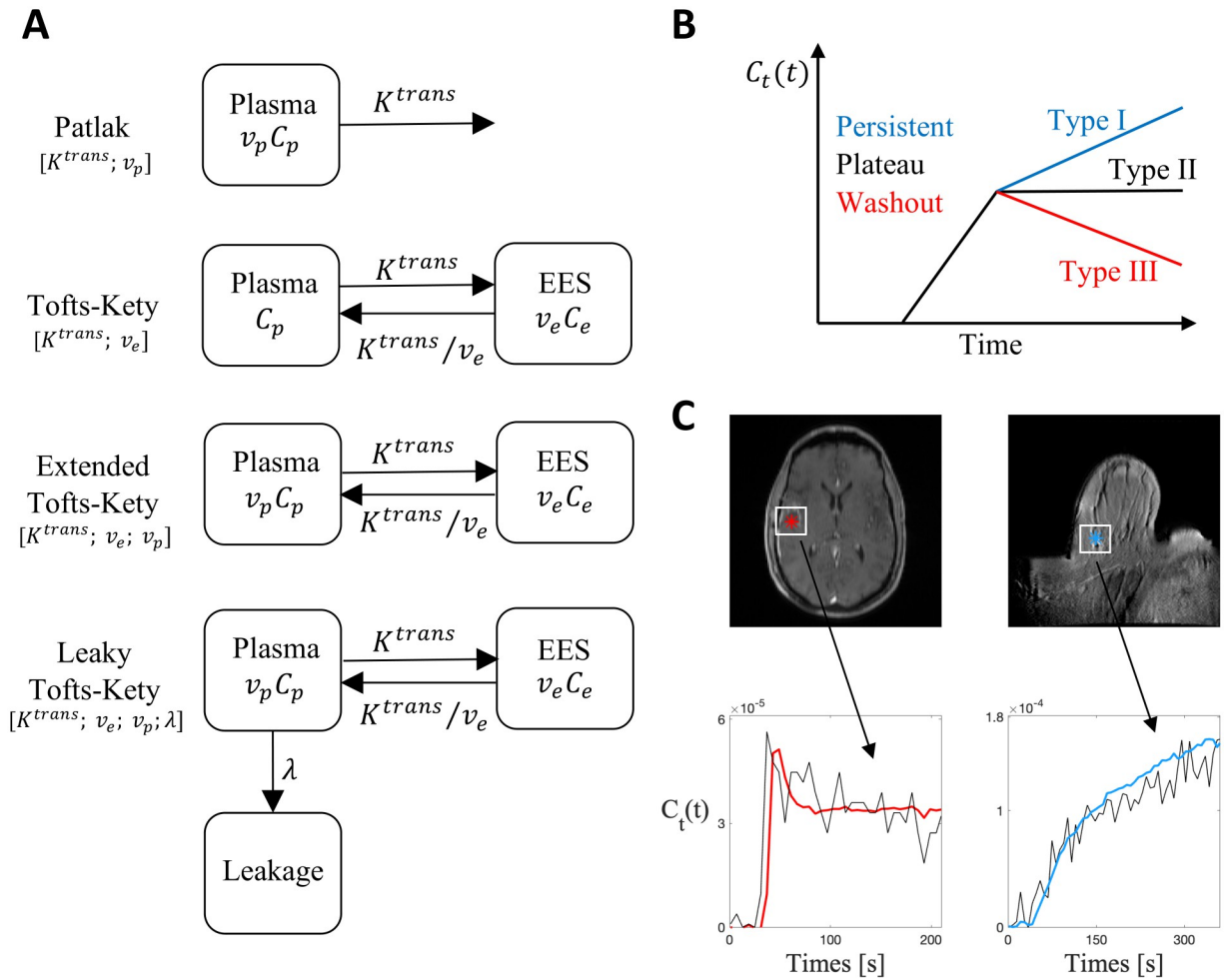
A

B

C

Fig 1. Models and data. (**A**) Schematic illustrations of the four nested transport models from simple (Patlak) to complex (Leaky Tofts–Kety): the contrast agent concentration $C_t(t)$ is evaluated using the functions $C_p(t)$, the CA concentration in the plasma compartment, which is assumed to be given by the arterial input function, and $C_e(t)$, for the CA concentration in the EES space. The rate of forward and backward volume transfer and the fractional EES and plasma volumes are the quantities K^{trans}, v_e, v_p, and λ. For each model, the involved parameters are listed in brackets. (**B**) Different enhancement patterns of CA signal: Type I—*persistent curve*—is a progressive increasing intensity signal; Type II—*plateau curve*—is characterized by an initial peak followed by a relatively constant enhancement; Type III—*wash-out curve*—refers to a sharp uptake followed by an enhancement decrease over time. (**C**) Examples of Type I (right plot) and Type III (left plot) enhancement curves obtained from breast and brain tumors, respectively.

For the evolution of the CA concentration in the EES compartment, and, thus, to derive the expression for $C_t(t)$, we analyze a class of nested compartmental models consisting of the Patlak model (PM), Tofts–Kety (TK) and its extended version (eTK), and the Leaky Tofts–Kety (LTK) model. The Patlak model, firstly introduced in [27], represents the simplest tissue uptake model and it assumes that CA diffuses from the PS to the EES at a rate governed by the forward transfer constant K^{trans}. It neglects the reflux from the EES back into the plasma space due to the assumption on low permeability and short measuring time. Thus, the concentration into the EES compartment varies according to

$$v_e \frac{dC_e}{dt} = K^{trans} C_p \tag{4}$$

and, assuming that the initial concentration in the EES is zero ($C_e(0) = 0$), from Eq (1), the tissue CA concentration is given by

$$C_t(t) = v_p C_p(t) + K^{trans} \int_0^t C_p(\tau) d\tau \qquad (5)$$

To overcome the low permeability hypothesis of the Patlak model the Tofts–Kety model was introduced in [28, 29]. The TK model accounts for bidirectional transfer of the contrast agent from the plasma to the EES compartment at rates governed by the forward transfer constant K^{trans} and the reverse constant $K_{ep} = K^{trans}/v_e$, respectively. However, it ignores the intravascular (plasma) compartment contribution (i.e., $v_p \approx 0$). The dynamics of the CA concentration in the EES compartment are described by

$$v_e \frac{dC_e}{dt} = K^{trans} \left(C_p - \frac{C_e}{v_e} \right). \qquad (6)$$

The transfer constant K^{trans} now has a different physiologic interpretation, depending on the balance between capillary permeability and blood flow: in high-permeability situations, K^{trans} is equal to the blood plasma flow per unit volume of tissue; in low permeability scenarios, K^{trans} is equal to the permeability surface area product between blood plasma and the EES, per unit volume of tissue [29]. Under the assumption that $v_p \approx 0$ and setting the initial concentration in the EES to zero ($C_e(0) = 0$), we can derive from Eq (1) the expression of the tissue CA concentration as

$$C_t(t) = K^{trans} \int_0^t C_p(\tau) \exp\left(-K_{ep}(t - \tau)\right) d\tau. \qquad (7)$$

The hypothesis of tissue being weakly vascularized ($v_p \approx 0$) may be invalid in some situations, especially in the case of highly vascular tumors. Thus, a modification of the TK model was proposed in [30]. Known as the extended Tofts–Kety model, it includes the vascular contribution $v_p C_p(t)$ to the overall CA tissue concentration, maintaining the same dynamics shown in Eq (6) for the EES concentration $C_e(t)$:

$$C_t(t) = v_p C_p(t) + K^{trans} \int_0^t C_p(\tau) \exp\left(-K_{ep}(t - \tau)\right) d\tau. \qquad (8)$$

The TK and eTK models have experienced some problems to obtain reliable estimation for the involved parameters when the data depict a persistent uptake curve (Type I) [31]. The PM model, with its assumption on unidirectional flux from the plasma to the EES compartment, is able to overcome this issue, but assuming a negligible reflux from the EES back into the plasma space is not realistic, especially in the high permeability regime [32]. The Leaky Tofts–Kety (LTK) model was introduced to address this issue [31]. The LTK model, also known as Leaky Tracer Kinetic model (LTKM), adds an additional compartment, the leakage compartment, to the already described plasma and permeable compartments. The permeable space and the leakage space are considered subcompartments of the EES region. The former assumes a bidirectional exchange between plasma and EES, while the latter considers a unidirectional flow from which the contrast, at a concentration $C_L(t)$, does not flow back into the vasculature. Thus, for the LTK model, the overall CA tissue concentration is given by

$$C_t(t) = v_p C_p(t) + v_e C_p(t) + C_L(t).$$

The contrast agent in the permeable compartment $C_e(t)$ evolves following Eq (6), while the

rate of contrast change in the leakage space can be read as

$$\frac{dC_L}{dt} = \lambda C_p \, .$$ (9)

Here, λ is the volume transfer constant from the plasma compartment to the leakage compartment. Assuming that the initial concentration in the EES and leakage compartments are zero ($C_L(0) = C_e(0) = 0$), then the CA tissue evolution is given by

$$C_t(t) = v_p C_p(t) + K^{trans} \int_0^t C_p(\tau) \exp\left(K_{ep}(t - \tau)\right)d\tau + \lambda \int_0^t C_p(\tau)d\tau.$$ (10)

In summary, the main differences between these models are the directional flows for the CA exchange between the plasma space, the extravascular extracellular space, and eventually the leakage space. The Patlak model is a unidirectional model which assumes CA transfer from EES to PS is negligible due to low permeability and short measurement time [27]. The Tofts–Kety model assumes that the CA diffuses from, and returns to the PS, and the vascular (plasma) compartment contribution is negligible [28]. This assumption of tissue being weakly vascularized is overcome with the extended Tofts model, which includes the vascular contribution to the tissue concentration [30]. Finally, the Leaky Tofts–Kety model extends the eTK, adding an additional leakage compartment with unidirectional flow for disease applications such as gliomas, where slow accumulation of CA from neighboring voxels is common [31]. In all models where the vascular component is considered, it is assumed that the concentration of the contrast agent within the vasculature is not affected by local transport, (i.e. it is an empirical forcing function), and that the difference between the empirical vascular input function and the local tissue concentration is the primary driver of transport between tissue and vasculature.

2.3 Data

Two DCE-MRI scans were used in this study. A brain scan was obtained from a patient with pathology-confirmed diagnosis of glioblastoma who underwent MRI at City of Hope National Medical Center. The T1-weighted brain DCE-MRI scan was acquired as follows: TR = 5.1ms, TE = 2.1ms, variable flip angle, with field of view 240mm x 240mm, matrix size 128x128 and image size 256 x 256 with 12 slices with slice thickness 6mm, and a temporal resolution of 6.03 seconds with 32 dynamic phases and 3 baseline images prior to contrast administration. A breast DCE-MRI scan was obtained from the Quantitative Imaging Network (QIN) BREAST-02 study, UPN-01. The image acquisition details for the breast MRI can be found in the documentation for the BREAST-02 study [33, 34]. In both cases, a variable flip angle (VFA) scan was acquired for direct contrast agent quantification [35]. The VFA scan was used to calculate the baseline T1 relaxation, T_{10}, of the tissue, which is used for calculating the local contrast agent concentration [36].

2.4 Identifiability analysis

Identifiability analysis is a fundamental mathematical tool used to assess a model's capability to describe data with unique determined parameters. It focuses on whether it is possible to identify a unique vector of parameter values for a given model structure, or whether multiple parameter values will fit the data equally well. It is important to distinguish between *structural identifiability*, which concerns how the model structure itself affects the possible unique identification of the involved parameters, and *practical identifiability*, which is based on the analysis of the model's ability to estimate parameters from the data with adequate precision.

Structural non-identifiability implies practical non-identifiability: in fact, if a model is not structurally identifiable, then the quality of the data collected does not matter; it will not be possible to uniquely estimate parameters in practice. The converse, however, is not true. Structural identifiability implies practical identifiability only when there is availability of infinitely resolved data, with zero measurement noise. However, even if the model structure theoretically allows parameters to be estimated, one still needs to have the appropriate data to achieve practically identifiable parameters.

2.4.1 Theory for structural identifiability analysis. Consider a dynamical system

$$\begin{cases} \dot{\mathbf{x}} = f(t, \mathbf{x}(t), \mathbf{u}(t), \boldsymbol{\theta}) \\ \mathbf{y}(t) = h(\mathbf{x}(t), \mathbf{u}(t), \boldsymbol{\theta}) \end{cases} \tag{11}$$

where $\mathbf{x}(t) \in \mathbb{R}^n$ represents the state variables, $\mathbf{y}(t) \in \mathbb{R}^m$ the measurable output (e.g., the data), $h(\cdot)$ the function that maps the states $\mathbf{x}$ to the observations $\mathbf{y}$, $\mathbf{u}(t) \in \mathbb{R}^r$ the external input function (in our case the vascular input function), and $\boldsymbol{\theta} \in \mathbb{R}^q$ the set of constant parameters. The dynamical system is structurally identifiable if each element θ_i of the vector $\boldsymbol{\theta}$ is structurally identifiable. This means that each of these elements can be uniquely determined from a given input $\mathbf{u}(t)$ and a measurable output $\mathbf{y}(t)$, i.e.,

$$\mathbf{y}(\mathbf{x}(t), \mathbf{u}(t), \boldsymbol{\theta}) = \mathbf{y}(\mathbf{x}(t), \mathbf{u}(t), \boldsymbol{\theta}') \Rightarrow \theta_i = \theta_i' \quad \forall i = 1, .., q$$

Alternatively, one element θ_i of the parameter vector $\boldsymbol{\theta}$ is structurally non-identifiable if varying its value does not necessarily alter the model trajectory $\mathbf{y}$, as these changes can be compensated for by varying other parameters. In particular, a model is defined to be structurally identifiable if all of its parameters are structurally identifiable [37]. A large variety of methods exist to assess structural identifiability of a system, from the Laplace transform [38], Taylor series expansion [39], seminumerical approaches [40, 41], differential algebra [42–44], and numerical algebraic geometry [45], among others (for reviews of some of these approaches, see Refs. [16, 46, 47]). Due to the simple structure of the nested models considered in this analysis and described in Section 2.2, we apply a differential algebra approach. This approach is convenient for linear compartmental models because of the reduced number of state variables (i.e., $C_t(t)$) and the direct relationship between state variables and observations (which actually coincides for this class of nested models). Further, this approach directly allows for testing identifiability, obtaining simple forms of possible identifiable combinations of the parameters, and identifying reparameterizations of the model when it is structurally non-identifiable.

2.4.2 Theory of practical identifiability. As already briefly explained, a parameter that is structurally identifiable may still be practically non-identifiable. This issue arises frequently if the quantity and/or quality of the experimental data is insufficient. Assessing the practical identifiability of a model (or a parameter) is fundamental in obtaining reliable parameter estimations and, thus, for ensuring good model prediction capabilities. While the notion of practical identifiability is not uniquely defined in the literature, we consider a definition based on the concept of profile likelihoods and confidence intervals [48]. Using this framework, we evaluate the agreement between the experimental data and the observable predicted by our set of nested models choosing as Maximum Likelihood Estimator (MLE) the objective (or cost) function defined as:

$$MLE(\boldsymbol{\theta}) = \frac{1}{\sigma^2} \sum_{i=1}^{N} \left(y_i^D - y_i^M(x(t_i), u(t_i), \boldsymbol{\theta})\right)^2 .$$

Here, N is the number of time points t_i available from the data, y_i^D are the CA data values at

time t_i, $y_i^M(x(t_i), u(t_i), \boldsymbol{\theta})$ is the CA value at time t_i predicted by the model with the estimation $\boldsymbol{\theta}$ of the parameter vector, and σ is the standard deviation of the noise of the data. In particular, this standard deviation is estimated as the inverse of the Signal-To-Noise (SNR) ratio of the data [21]. The state variable $x(t)$ represents the CA concentration $C_t(t)$ and $u(t)$ is the vascular input function. The parameter vector $\hat{\boldsymbol{\theta}}$ used to evaluate the practical identifiability of the model is given by

$$\hat{\boldsymbol{\theta}} = \arg\ \min[MLE(\boldsymbol{\theta})]\,.$$

To determine the confidence interval of the estimated set of parameter $\hat{\boldsymbol{\theta}}$, we consider the profile likelihood (PL) method. To build the profile likelihood plot, the idea is to choose one parameter θ_i, vary its value around the maximum likelihood estimate $\hat{\theta}_i$, and re-optimize the remaining parameters. Thus, the profile likelihood is given by

$$PL(\theta_i) = \min_{\theta_{j \neq i}}\ [MLE(\boldsymbol{\theta})].$$

Then, the confidence intervals (CI) of estimated parameters are defined as

$$CI_{PL}(\theta_i) = \{\theta_i | PL(\theta_i) \leq MLE(\hat{\boldsymbol{\theta}}) + \Delta_\alpha\}$$

where Δ_α represents the α-th quantile of the chi squared (χ^2) distribution with $k = 1$ degrees of freedom for a point-wise confidence interval [37, 49]. Thus, given the optimal value $\hat{\theta}_i$ of one parameter, defining the confidence interval to a confidence level α implies that the true value $\hat{\theta}_i$ of the parameter is located within this interval with probability α. When this confidence interval is finite, then a parameter θ_i is practically identifiable. Otherwise, if the confidence region is infinitely extended, although the numerical algorithm finds a unique minimum $\hat{\boldsymbol{\theta}}$, then the parameter is practically non-identifiable. Precisely, we analyze the profiles of the $MLE(\hat{\boldsymbol{\theta}})$ versus each parameter θ_i. The choice of a least squares function for the MLE is equivalent to working with an additive Gaussian noise measurement model with constant variance. We point out the reader that the assumption of additive Gaussian noise may not be the more appropriate under certain conditions, especially for data close to zero. We highlight that other choices of measurement error model may be considered in order to relax this assumption of additive Gaussian noise (see [50] for a recent review on the topic). In any case, the method of the profile likelihood analysis here implemented holds when different measurement models are used.

A structurally non-identifiable parameter is characterized by a flat profile likelihood, whereas the profile likelihood of a practically non-identifiable parameter may have a minimum, but does not have a well-defined confidence level α for increasing and/or decreasing values of θ_i. Instead, for an identifiable parameter the profile likelihood exceeds such threshold in both directions of θ_i. Fig 2 shows an illustrative example of likelihood profiles. Practical identifiability as determined by profile likelihoods methods are standard methods for determining the unique parametrization of a real-world model-data pairing. We refer the interested reader to [37] for a detailed primer on profile likelihoods and practical identifiability. Profile likelihood-based confidence intervals are often used in biological applications to ensure that there is sufficient data and data quality to assume the validity of the model [14, 51–54]. With respect to other methods for determining confidence intervals, this particular method allows for asymmetric intervals that are invariant under re-parametrizations of the model. The analysis performed here refers to univariate likelihood profiles, where we are considering only one target parameter. For the reader convenience, it is worthy to mention that other options are available
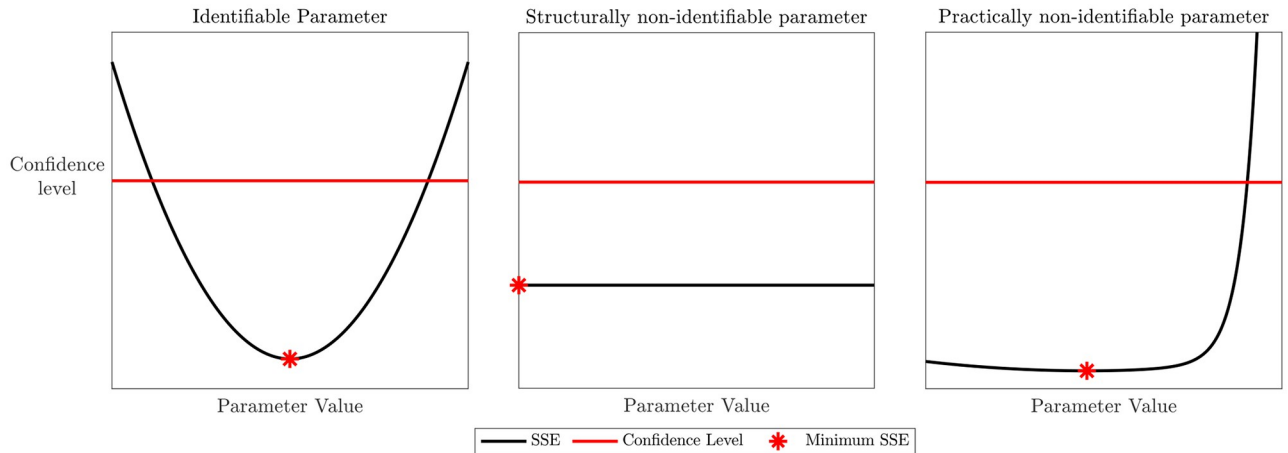
Fig 2. **Illustrative example of profile likelihood for an identifiable parameter and structurally and practically non-identifiable parameters.**

when pairs (or more) target parameters are considered. In particular, in this cases bivariate or higher-order profiles can be generated and studied [53].

In addition to the profile likelihood, we also analyze the compensating profiles of the model parameters. These are obtained by perturbing one parameter θ_i around its maximum likelihood estimate $\hat{\theta}_i$ and plotting the variation of the re-optimized parameters versus the perturbed θ_i value. This analysis demonstrates how a non-identifiable parameter (whether structural or practical), may be compensated for by variations of other parameters. The small dimensionality of our systems allows us to use the described method for the analysis proposed in Section 3.2. We analyze the practical identifiability for the family of nested models described in Section 2.2 using a self-implemented code in Matlab based on the Particle Swarm algorithm for global optimization [55, 56]. The codes used for the analysis proposed in these notes are available in the corresponding GitHub repository: https://github.com/mconte93/Practical_Identifiability.git.

3 Results

Here we analyze the results concerning structural and practical identifiability of the most complex of the nested models, the LTK model described in Section 2.2.

3.1 Structural identifiability of the LTK model

Following the formalism of the differential algebra approach described in Section 2.4.1, model (10) can be rewritten as

$$
\begin{cases}
v_e \dot{x}_1 = K^{trans}\left(u - \dfrac{x_1}{v_e}\right) \\[2mm]
\dot{x}_2 = \lambda u \\[2mm]
y = v_e x_1 + v_p u + x_2
\end{cases}
\tag{11}
$$

where y is the observable concentration of the contrast agent in the tissue $C_t(t)$, $u(t)$ is the external input given by the concentration of contrast agent in the plasma compartment (i.e., $C_p(t)$ in (2)), x_1 and x_2 are the state variables for the CA concentration into the EES and leakage

compartment, respectively. Differentiating the last equation in system (11) and plugging inside the first two equations of (11), we obtain the differential equation for $y(t)$ of the form

$$\dot{y} + a_1 y + a_2 u + a_3 \dot{u} + a_4 v = 0 \tag{12}$$

where v is defined as $v = \int_0^t u(\tau)d\tau$ and the coefficients a_i are given by

$$\begin{cases} a_1 = \dfrac{K^{trans}}{v_e^2} \\[3mm] a_2 = -K^{trans} - \dfrac{K^{trans}}{v_e^2} - \lambda \\[3mm] a_3 = -v_p \\[3mm] a_4 = -\dfrac{K^{trans}}{v_e^2}\lambda \end{cases} \tag{13}$$

We observe that $a_2, a_3, a_4 < 0$, while $a_1 > 0$. Solving system (13) for the four parameters of the LTK model provides the following expressions:

$$\begin{cases} K^{trans} = \dfrac{a_4}{a_1} - a_1 - a_2 \\[3mm] v_e = \sqrt{\dfrac{a_4}{a_1^2} - 1 - \dfrac{a_2}{a_1}} \\[3mm] v_p = -a_3 \\[3mm] \lambda = -\dfrac{a_4}{a_1} \end{cases} \tag{14}$$

For v_e to be well-defined we need $a_2 \leq \dfrac{a_4}{a_1} - a_1$, which always holds as the four parameters of the LTK model are positive. From this analysis, we can conclude that LTK model is structurally identifiable. The structural identifiability of the nested PM, TK, and eTK models has also been analyzed and details are provided in S1 Text. Moreover, for the reader's convenience, in S2 Text we provide an example of a structurally non-identifiable model obtained by modifying the LTK model structure and changing the connections among the compartments.

3.2 Practical identifiability of the LTK model

Practical identifiability is performed using the method described in Section 2.4.2 and results are compared with the analytical results obtained in Section 3.1 regarding parameter structural identifiability. Precisely, we study the effect of varying the noise characteristics of the DCE-MRI data used for estimating the VIF and CA concentration on the accuracy of the identification of the model parameters. Each analysis is performed on the three characteristic enhancement patterns observed in CA evolution [10] (Fig 3). As shown in Fig 1B, CA time-enhancement curves are classified into three types: Type I—*persistent* curve—a progressive signal intensity increase (Fig 1C, right plot); Type II—*plateau* curve—is characterized by an initial peak followed by a relatively constant enhancement; Type III—*wash-out* curve—refers to a sharp uptake followed by an enhancement decrease over time (Fig 1C, left plot). We consider two different tissues to study the role of the tissue characteristics on model identifiability. In both tissues, we replicate the analysis for the three different CA time-enhancement curves. We report results on the Glioblastoma multiforme (GBM) brain tumor data in the main text.
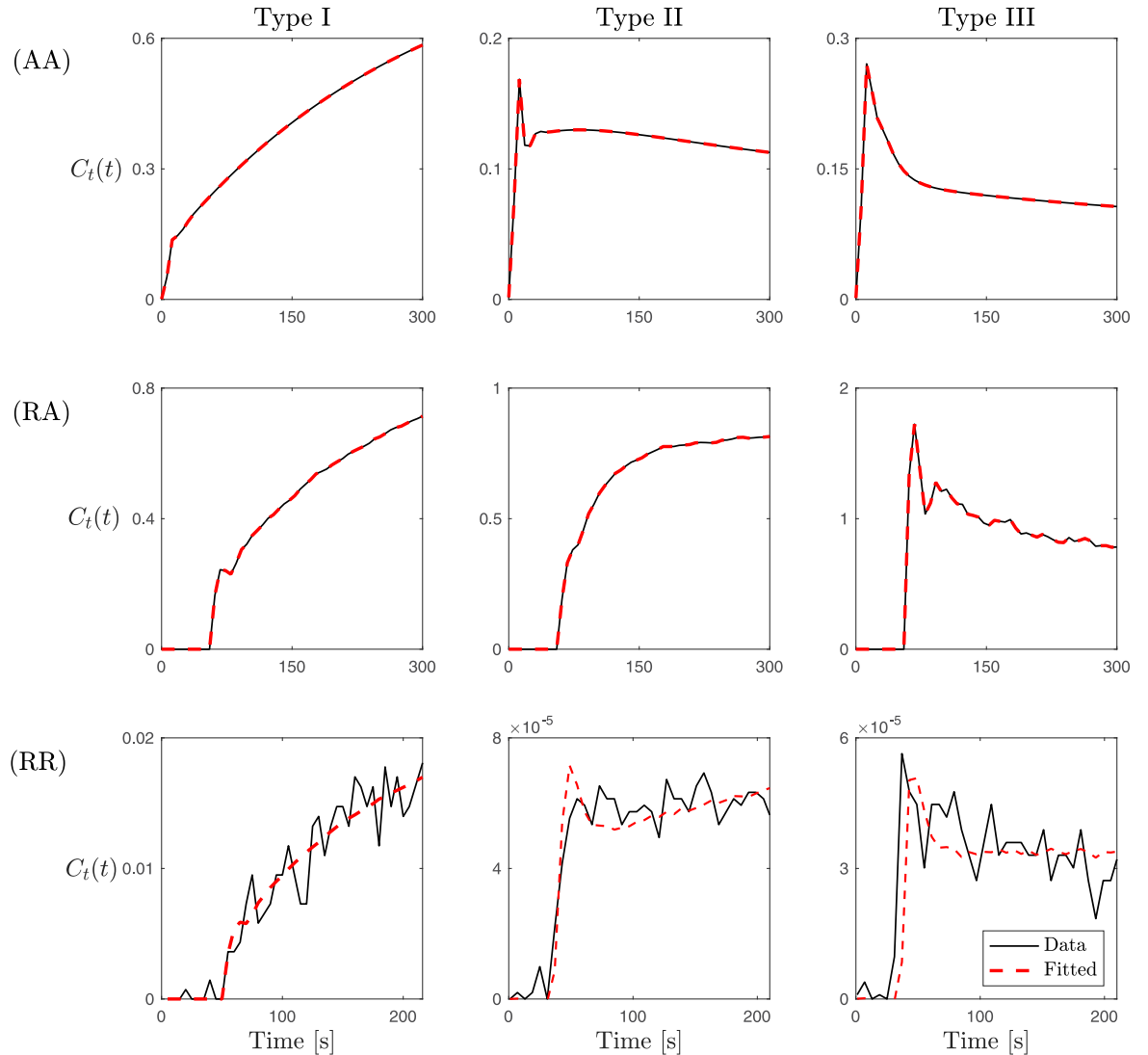
Fig 3. Best fitting of CA evolution signal obtained with the LTK model (10). The three types of CA time-enhancement curves (columns) for the three cases of study (AA), (RA), and (RR) (rows). The last row (RR) is CA time course data from the GBM DCE-MRI. Similar results for the breast cancer dataset are provided in Fig C in S3.1 Text.

https://doi.org/10.1371/journal.pcbi.1012106.g003

Results for the breast cancer data are presented in S3.1 Text. For practical identifiability analysis we distinguish between the following three cases of study (referring to the rows of Fig 3).

(AA). The first case is referred to as *Artificial-Artificial*. Here, we consider an *artificial* VIF given analytically by Eq (3) and three *artificial* data sets. These are generated by running forward simulations of the LTK model, given by Eq (10), with the parameter values listed in Table 1, and replicate the three CA time-enhancement curves. In particular, these artificial data sets represents noise-free experimental data. Thus, in this case, there is no noise in the VIF or in the data which could affect the parameter identifiability. For the VIF we set $A_1 = 48.54$ mM × s, $A_2 = 18.64$ mM × s, $\sigma_1 = 3.378$ s, $\sigma_2 = 7.92$ s, $T_1 = 10.2276$ s, $T_2 = 21.9$ s, $\alpha = 1.05$ mM, $\beta = 0.0028$ s^{-1}, $l = 0.6346$ s^{-1}, and τ = 28.98 s.

Table 1. Parameter values used for the synthetic data set in the (AA) case.

Type	K^{trans} (s^{-1})	v_e	v_p	λ (s^{-1})
I	0.0025	0.9	0.05	0.01
II	0.009	0.5	0.1	0.001
III	0.03	0.5	0.1	0.001

(RA). The second case is referred to as *Real-Artificial*. Here, we consider a *real* estimation of the VIF directly from DCE-MRI data by drawing a ROI around a major vessel, and three *artificial* data sets. These are obtained by running forward simulations of the LTK model, given by Eq (10), with the parameter values listed in Table 2 and the *real* VIF. This *real* VIF includes noise, as compared to the analytic expression for the *artificial* VIF as in the (AA) case.

(RR). The last case is referred to as *Real-Real*. Here, we consider both a *real* estimation of the VIF and a *real* evolution of the contrast agent in the tissue. We analyze data from a GBM brain tumor and a breast cancer MRI dataset.

The three CA time-enhancement curves used in (AA), (RA), and (RR) cases are shown in Fig 3 (continuous black lines) together with the corresponding model fits obtained with the LTK model (10) (dashed red lines). The particle swarm (PS) method is used to estimate parameter values for fitting the three curve types and in the three cases of study (AA), (RA), and (RR). Values of fitted parameters are collected in Table A in S3 Text.

Recalling the methodology described in Section 2.4.2, we analyze profile likelihood and confidence levels for each of the parameters involved in the LTK model, in the three cases of study (AA), (RA), and (RR), and for the three types of CA time-enhancement curves. Here, we report the results for the Type I enhancement curve, as the LTK model was introduced with the aim of solving the issues of PM, TK, and eTK models concerning parameter estimation for persistent uptake CA profile. Results concerning Type II and Type III time-enhancement curves are collected in Figs A and B in S3 Text. Moreover, we show the results for K^{trans} and λ parameters. K^{trans} is the only parameter appearing in all nested models analyzed in this study, thereby allowing for a direct comparison of the results obtainable with the different models. λ is a novel parameter from the LTK model, thus it is important to analyze its identifiability.

Fig 4 shows the results concerning practical identifiability of the parameter K^{trans} for the LTK model and Type I time-enhancement curve. The columns of Fig 4 refer to the three cases of study (AA), (RA), and (RR). From Section 3.1, we know that K^{trans} is a structurally identifiable parameter, i.e., it is possible to uniquely determine its value from the given model structure. When we consider a completely artificial data set, obtained with the parameter values collected in Table 1 and the population-based analytical expression of the VIF given in (3), the complete absence of noise in the data and in the VIF allows us to accurately recover K^{trans}. In

Table 2. Parameter values used for the synthetic data set in the (RA) case of study.

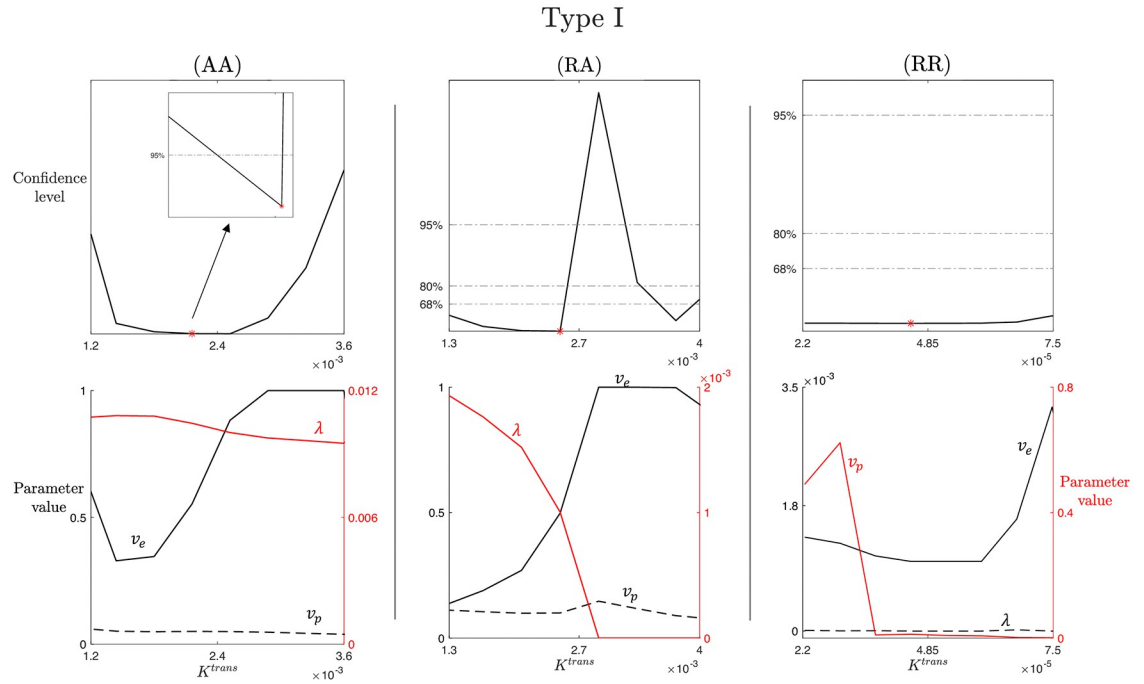| Type	K^{trans} (s^{-1})	v_e	v_p	λ (s^{-1})
I	0.0025	0.9	0.05	0.001
II	0.009	0.5	0.1	0.001
III	0.008	0.001	0.9	0

Fig 4. K^{trans} practical identifiability for LTK model and Type I enhancement curve. Top row: profile likelihood and confidence levels at 68%, 80%, and 95% for the parameter K^{trans} in the (AA), (RA), and (RR) case for the Type I enhancement curve. Inset in the first subplot shows a zoom of the region around the best-fitted value $\hat{K}^{trans}$ (red marker). Bottom row: compensating profiles of the parameters v_e, v_p, and λ with respect to variation of K^{trans} around its best-fitted value. Variation of ±50% around the optimal value of K^{trans} are considered. Two colors are for two different y-axis: black curves refer the left y-axis and red curves to the right y-axis. Different line styles are used to distinguish curves referring to the same y-axis. For each curve, the name of the corresponding parameter is indicated above the line in the same color.

https://doi.org/10.1371/journal.pcbi.1012106.g004

the (AA) case, the profile likelihood shows a well-defined parabola, with a unique minimum in the optimal value $\hat{K}^{trans}$. Zooming around this minimum, we observe a finite confidence region around $\hat{K}^{trans}$ for the 95% confidence level. Analyzing the (RA) case (second column), we notice that $\hat{K}^{trans}$ represents a local minimum for the profile likelihood and it is not possible to identify a lower bound for the confidence regions for both 95%, 80%, and 68%, i.e., it is not possible to define a finite confidence interval. Thus, K^{trans} is practically non-identifiable in this case. Moreover, from the compensating profiles in the region where the profile likelihood is almost flat (left side with respect to $\hat{K}^{trans}$), we notice v_e and λ compensating for varying K^{trans}. In contrast, the optimal value estimated for v_p does not significantly changes with respect to K^{trans} variation. This is in line with the results in (13), where we can notice how v_p does not have any relation with K^{trans}. In the (RR) case, K^{trans} is not practically identifiable, evident from the flat likelihood profile, which makes it not possible to identify a lower or upper bound of a confidence region with respect to the optimal value $\hat{K}^{trans}$.

Similar observations can be made from the results of Fig 5, where practical identifiability of the parameter λ for the LTK model and Type I time-enhancement curve is analyzed. As for Fig 4, columns of Fig 5 refer to the three cases (AA), (RA), and (RR). From the structural identifiability analysis of Section 3.1, we know that λ is a structurally identifiable parameter, thus, it is possible to uniquely identify its value from the model structure. For the completely artificial data set used in (AA), we are able to accurately identify λ. The profile likelihood in the first subplot of Fig 5 shows a well-defined parabola with a unique minimum in the optimal value $\hat{\lambda}$,
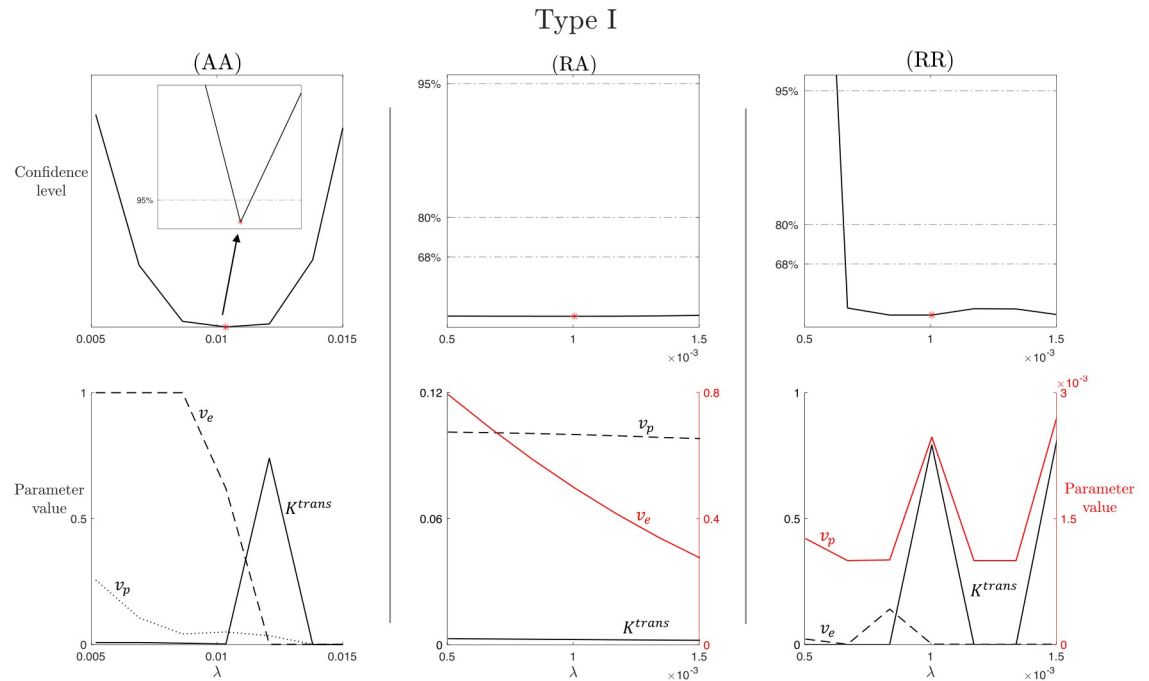
Fig 5. Leakage (λ) practical identifiability for LTK model and Type I enhancement curve. Top row: profile likelihood and confidence levels at 68%, 80%, and 95% for the parameter $K\lambda$ in the (AA), (RA), and (RR) case for the Type I enhancement curve. Inset in the first subplot shows a zoom of the region around the best-fitted value $\hat{\lambda}$ (red marker). Bottom row: compensating profiles of the parameters K^{trans}, v_e, and v_p with respect to variation of λ around its best-fitted value. Variation of ±50% around the optimal value of λ are considered. Two colors are for two different y-axis: black curves refer the left y-axis and red curves to the right y-axis. Different line styles are used to distinguish curves referring to the same y-axis. For each curve, the name of the corresponding parameter is indicated above the line in the same color.

around which a finite confidence region for the 95% confidence level can be determined (as shown in the zoomed inset). Analyzing the RA and RR cases (second and third columns), we notice that the profile likelihood is characterized by flat regions for which it is not possible to identify a lower or upper bound for 95%, 80%, and 68% confidence levels. Thus, λ is not practically identifiable in these more realistic cases. Looking at the corresponding compensating profiles, we observe that v_p estimation is not influenced by λ variation, while v_e and K^{trans} show variability in response to λ. This result is reasonable in relation to the results in (14): the expression for v_p is independent from the other parameters, whereas K^{trans}, v_e, and λ expressions depends on common coefficients (i.e., a_1, a_2, and a_4).

Observation 1. *For reader convenience, we point out that it is reasonable to obtain different optimal estimations for K^{trans} in the different analyzed cases (AA, RA, RR), as moving from AA to RA and, then, RR case, we are changing the VIF and the DCE data on which the inverse problem is performed.*

To specifically analyze the influence of the noise in both the data and the individual-based estimation of the VIF function, derived directly from the DCE-MRI data, we perform two different tests, whose results are shown in Figs 6 and 7. We first analyze the impact of increasing the noise in the VIF function, mimicking the process that leads from the AA to the RA case. In fact, the individual-based estimations of the VIF are characterized by a predefined level of noise that is not present in the analytical VIF estimations. To this aim, we define three different amplitudes for the noise-only signal, corresponding to the 5%, 10%, and 15%, respectively, of
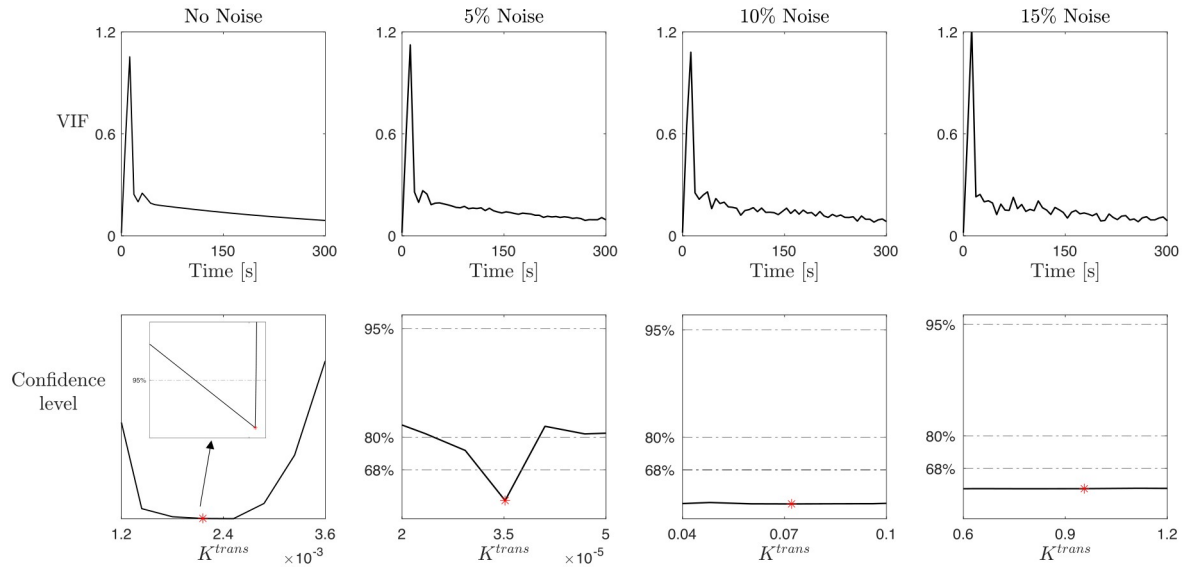
Fig 6. Study on the noise effect on parameter practical identifiability in the LTK model. Top row: Artificial VIF obtained from the analytical expression (Eq (3)) by adding a noisy signal with increased amplitudes. No noise VIF (first subplot) is the artificial VIF used in the (AA) case, while 5%, 10%, and 15% noise VIF (second to fourth subplots) are obtained by adding noise to the noise-free VIF. Bottom row: profile likelihood and confidence levels at 68%, 80%, and 95% for the parameter K^{trans} for a Type I enhancement curve obtained by repeating the study on K^{trans} with the increasing noisy VIF illustrated in the top row. Red markers indicate the best-fitted value $\hat{K}^{trans}$.

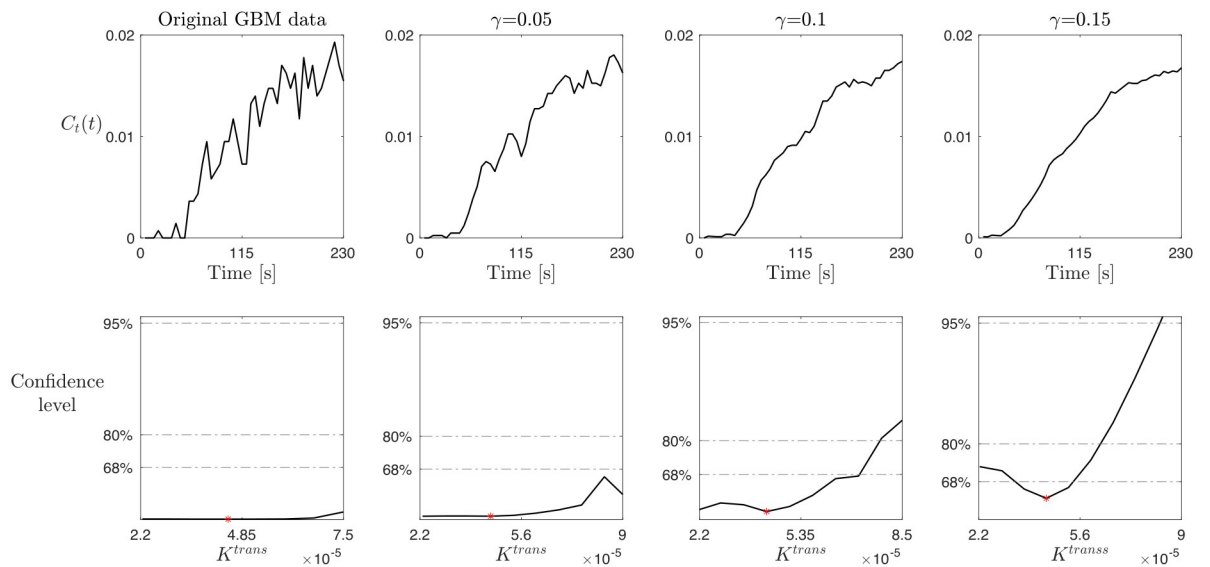https://doi.org/10.1371/journal.pcbi.1012106.g006

Fig 7. Study on the smoothing effect on parameter practical identifiability for the LTK model. Top row: CA profile obtained from the GBM data in a Type I enhancement curve by smoothing the data using a moving average method with different values of the smoothing factor γ, i.e., $\gamma = 0.05$ (second column), $\gamma = 0.1$ (third column), and $\gamma = 0.15$ (fourth column). The original GBM data (first column) are the same used in the (RR) case. Bottom row: profile likelihood and confidence levels at 68%, 80%, and 95% for the parameter K^{trans} obtained by repeating the study on K^{trans} with the smoothed data illustrated in the top row.

https://doi.org/10.1371/journal.pcbi.1012106.g007

the noise-free VIF at every element. These amplitudes allow to control the amount of noise. Then, we define the noise-only signal in the form a standard normal distribution. Finally, we add the noise-only signal adjusted with the corresponding amplitude to your original noise-free VIF. This creates the noisy VIF used in the study. More details can be found in the available code. Fig 6 shows the results of this analysis for the parameter K^{trans} and Type I time-enhancement curve. Analogous results can be obtained for the other parameters and enhancement profiles. The first column, the no noise case, replicates the same results shown in the first column of Fig 4, i.e., the practical identifiability of K^{trans} with a confidence level of 95%. Increasing the noise in the VIF, up to 5%, we observe that K^{trans} is still practically identifiable, but with a lower confidence level (80%). Considering higher levels of noise of the VIF (10% or 15%), the practical identifiability of the parameter is no longer guaranteed, as the confidence region bounds become no longer finite for the considered confidence levels. This supports the conclusion that increasing noise in the VIF decreases the confidence level of parameter identifiability, justifying the differences in the results between (AA) and (RA) cases in Figs 4 and 5.

To analyze the influence of the noise in CA data on the parameter identifiability and, thus, mimicking the process that leads from the RR to the RA case, we perform a second test based on data smoothing. Starting from the CA time evolution data from the GBM dataset for a Type I time-enhancement curve, we use a moving average method with different values for the smoothing factor γ. Precisely, the method is based on the moving average technique that slides a window along the data, computes the mean of the points inside of each window, and replaces each data point with the average of the neighboring data points defined within the span. The window size is fixed and heuristically determined by the algorithm depending on the input data, while $\gamma \in [0, 1]$ adjusts the level of smoothing by scaling the window size. Values of γ near 0 produce smaller moving window sizes, resulting in less smoothing, while values near 1 produce larger moving window sizes, resulting in more smoothing. Fig 7 summarizes the results of this analysis. The first column, referring to the original GBM data, replicates the same results shown in the last column of Fig 4, i.e., K^{trans} is not practically identifiable, with an almost flat profile likelihood. However, moving from left to right in Fig 7, the higher the value of the smoothing factor γ, i.e., the smoother the data, the less flat the corresponding profile likelihood. In particular, the last column of Fig 7, referring to $\gamma = 0.15$, shows the practical identifiability of K^{trans} can be recovered for the confidence level of 68%. We would not expect to obtain a higher confidence level for K^{trans}. These results justify the conclusion that high levels of noise in the data decrease the confidence level of parameter identifiability, in line with the previous shown results for RA and RR case in Figs 4 and 5.

4 Discussion

In this work, we have carried out a formal and in-depth study of the structural and practical identifiability of a well-known class of transport models widely used for the analysis of DCE-MRI data, with the aim of showing the impact of specific data characteristics on intrinsic features of these models. We focused on the LTK model, which accounts for the different aspects that are separately included in other members of the nested family of compartmental models under investigation. However, analysis for the entire nested family has been also carried out and the corresponding results are shown in the S1 Text.

In Sections 3.1 and S1.1 Text, we analyzed structural model identifiability, showing how in all PM, TK, eTK, and LTK models it is possible to define a unique parametrization that identifies the parameters through the given inputs, i.e., CA concentration $C_t(t)$ and vascular input function VIF. As a matter of completeness, in S2 Text, we also described an additional transport model of the same class—namely the mLTK model—which is not structurally identifiable,

but for which a structurally identifiable reparametrization can be defined. Then, in Section 3.2 and S1.2 Text, we used the method based on profile likelihood and confidence intervals to study practical identifiability of the nested family of models in three different scenarios, accounting for different levels of noise and construction of the data, and for different CA time-enhancement profiles. In fact, studying the practical identifiability of a model with respect to the data at hand is crucial for ensuring well-determined model predictions, as these are often used in systems biology research and quantitative image analysis.

The obtained results show how the entire class of transport models for DCE-MRI analysis, from PM to LTK, is structurally identifiable, i.e., they have an intrinsic mathematical structure that allows for a unique identification of the parameters and, thus, reproducible and accurate outcomes. However, practically this would happen only in the ideal case of dealing with a very large amount of data with zero noise. Our findings for both the LTK model (discussed in Section 3.2) and the nested PM, TK, and eTK models (discussed in S1.2 Text) reveal how practical parameter and, thus, model identifiability is affected by the quality of the data: the more noisy the data and/or the individual-based VIF function, the lower the confidence levels of identifiability of the different parameters. This is evident from the change in the shape of the profile likelihood transforming from a parabola-like shape in the (AA) case to a flat shape in the (RR) case, shown in Figs 4 and 5, and A (in S1.2 Text) for Type I contrast enhancement curve. The same changes in the profile likelihood shapes are observed for Type II (Fig A in S3 Text) and Type III (Fig B in S3 Text) contrast enhancement curves. These results support the observation that model identifiability is not attributed to a specific contrast agent dynamic, but rather to the characteristics of the data from which the enhancement curves are obtained. Moreover, the further analysis concerning the impact of noise and data smoothness on model identifiability, whose results are summarized in Figs 6 and 7, show how modifying the data directly affects on the profile likelihood shape (from a parabola to a flat profile and vice versa). In fact, results highlights how reducing the VIF noise or obtaining smoother data profiles (e.g. with higher temporal resolution) allows for recovery of parameter identifiability and, thus, increasing the reliability of the derived parameter values. Concerning limitations, all our results have been obtained using a global optimization procedure, which is based on a fixed discrete sampling of the parameter space and does not work perfectly with respect to real-world noisy data. Thus, possible extensions of this work might focus on comparing the performances of different optimizes, either in terms of parameter estimations, by varying the sampling frequency in parameter space, or algorithm efficiency.

The analysis proposed here is of significant importance considering the wide use of DCE-MRI data in research [10, 57] and, thus, the need for ensuring reliability and reproducibility of transport model results [58]. DCE-MRI has been shown to be associated with tumor angiogenesis and may be used to assess glioma grading [59–64], predict genetic mutation status of brain tumors [65–67], distinguish pseudoprogression from true progression in glioblastomas [68, 69], and predict response to antiangiogenic treatment [70]. The parameter K^{trans}, in fact, as a marker for tumor microvascular permeability from DCE analysis, could help to predict treatment response in glioblastoma [71]. Moreover, DCE-MRI parameters in a breast cancer study have been reported to be associated with microvessel density which is a marker for angiogenesis [72]. However, variability in DCE acquisition (e.g. in scan duration) and imaging analysis with various transport models may produce diverging results, which makes repeatability a challenging issue and hinders its wider adaptation for both clinical practice and research [58, 73]. Prospective longitudinal clinical trials, preferably in a multicenter setting with standardized imaging techniques and quantification of DCE parameters, are needed to validate the utility of transport parameters as imaging biomarkers for treatment response and survival prediction.

In this light, understanding model and data issues and limitations allows for a more conscious use of the results obtainable with them. Our results provide a mathematical explanation for the lack of repeatability of DCE-MRI quantification between clinical sites, as it has been previously reported [74]. As we have shown that practical identifiability improves with increasing SNR, we emphasize the need for image acquisition standards to increase the quality of imaging data and therefore reliability of parameter estimations such as the standards proposed by the Quantitative Imaging Biomarkers Alliance (QIBA) [75]. As DCE-MRI acquisition protocols and quantification methods continue to rapidly develop [76], it is important to ensure rigor in model fitting and analysis.

Supporting information

S1 Text. Identifiability of PM, TK and eTK models. It contains Fig A.
(PDF)

S2 Text. Modified Leaky Toft-Kety (mLTK): A structurally non-identifiable model. It contains Figs A and B.
(PDF)

S3 Text. Supplementary data for the LTK model. It contains Tables A and B and Figs A, B, C, D.
(PDF)

Acknowledgments

Author Contributions

Conceptualization: Martina Conte, Ryan T. Woodall, Russell C. Rockne.

Formal analysis: Martina Conte.

Funding acquisition: Christine E. Brown, Jennifer M. Munson, Russell C. Rockne.

Methodology: Martina Conte, Ryan T. Woodall, Russell C. Rockne.

Project administration: Russell C. Rockne.

Resources: Christine E. Brown, Jennifer M. Munson, Russell C. Rockne.

Supervision: Russell C. Rockne.

Writing – original draft: Martina Conte.

Writing – review & editing: Martina Conte, Ryan T. Woodall, Margarita Gutova, Bihong T. Chen, Mark S. Shiroishi, Christine E. Brown, Jennifer M. Munson, Russell C. Rockne.

References

1. Sorace AG, Partridge SC, Li X, Virostko J, Barnes SL, Hippe DS, et al. Distinguishing benign and malignant breast tumors: preliminary comparison of kinetic modeling approaches using multi-institutional

dynamic contrast-enhanced MRI data from the International Breast MR Consortium 6883 trial. J Med Imaging 2018; 5:11019–19 https://doi.org/10.1117/1.JMI.5.1.011019 PMID: 29392160

2. DiCarlo JC, Jarrett AM, Kazerouni AS, Virostko J, Sorace A, Slavkova KP, et al. Analysis of simplicial complexes to determine when to sample for quantitative DCE MRI of the breast. Magn Reson Med. 2023; 89:1134–50 https://doi.org/10.1002/mrm.29511 PMID: 36321574

3. Wu C, Jarrett AM, Zhou Z, Elshafeey N, Adrada BE, Candelaria RP, et al. MRI-based digital models forecast patient-specific treatment responses to neoadjuvant chemotherapy in triple-negative breast cancer. Cancer Res. 2022; 82:3394–404 https://doi.org/10.1158/0008-5472.CAN-22-1329 PMID: 35914239

4. Hormuth DA II, Farhat M, Christenson C, Curl B, Quarles CC, Chung C, et al. Opportunities for improving brain cancer treatment outcomes through imaging-based mathematical modeling of the delivery of radiotherapy and immunotherapy. Adv Drug Deliv Rev. 2022; 187:114367 https://doi.org/10.1016/j.addr.2022.114367 PMID: 35654212

5. Virostko J, Sorace AG, Slavkova KP, Kazerouni AS, Jarrett AM, DiCarlo JC, et al. Quantitative multiparametric MRI predicts response to neoadjuvant therapy in the community setting. Breast Cancer Res. 2021; 23:1–12 https://doi.org/10.1186/s13058-021-01489-6 PMID: 34838096

6. Fukumura D, Kloepper J, Amoozgar Z, Duda DG, and Jain RK. Enhancing cancer immunotherapy using antiangiogenics: opportunities and challenges. Nat Rev Clin Oncol. 2018; 15:325–40 https://doi.org/10.1038/nrclinonc.2018.29 PMID: 29508855

7. Cuenod C and Balvay D. Perfusion and vascular permeability: basic concepts and measurement in DCE-CT and DCE-MRI. Diagn Interv Imaging 2013; 94:1187–204 https://doi.org/10.1016/j.diii.2013.10.010 PMID: 24211260

8. Zhang W, Kong X, Wang ZJ, Luo S, Huang W, and Zhang LJ. Dynamic contrast-enhanced magnetic resonance imaging with Gd-EOB-DTPA for the evaluation of liver fibrosis induced by carbon tetrachloride in rats. PloS One 2015; 10:e0129621 https://doi.org/10.1371/journal.pone.0129621 PMID: 26076199

9. Materne R, Smith A, Peeters F, Dehoux JP, Keyeux A, Horsmans Y, et al. Assessment of hepatic perfusion parameters with dynamic MRI. Magn Reson Med. 2002; 47:135–42 https://doi.org/10.1002/mrm.10045 PMID: 11754452

10. Khalifa F, Soliman A, El-Baz A, Abou El-Ghar M, El-Diasty T, Gimel'farb G, et al. Models and methods for analyzing DCE-MRI: A review. Med Phys. 2014; 41:124301 https://doi.org/10.1118/1.4898202 PMID: 25471985

11. Wu C, Wang N, Gaddam S, Wang L, Han H, Sung K, et al. Retrospective quantification of clinical abdominal DCE-MRI using pharmacokinetics-informed deep learning: a proof-of-concept study. Front Radiol. 2023; 3 https://doi.org/10.3389/fradi.2023.1168901 PMID: 37731600

12. Choi KS, You SH, Han Y, Ye JC, Jeong B, and Choi SH. Improving the reliability of pharmacokinetic parameters at dynamic contrast-enhanced MRI in astrocytomas: a deep learning approach. Radiology 2020; 297:178–88 https://doi.org/10.1148/radiol.2020192763 PMID: 32749203

13. Liu Y, Suh K, Maini PK, Cohen DJ, Baker RE. Parameter identifiability and model selection for partial differential equation models of cell invasion. J R Soc Interface 2024; 21(212):20230607. https://doi.org/10.1098/rsif.2023.0607 PMID: 38442862

14. Simpson MJ, Browning AP, Warne DJ, Maclaren OJ, and Baker RE. Parameter identifiability and model selection for sigmoid population growth models. J Theor Biol. 2022; 535:110998 https://doi.org/10.1016/j.jtbi.2021.110998 PMID: 34973274

15. Villaverde AF, Barreiro A, and Papachristodoulou A. Structural identifiability of dynamic systems biology models. PLoS Comput Biol. 2016; 12:e1005153 https://doi.org/10.1371/journal.pcbi.1005153 PMID: 27792726

16. Villaverde AF. Observability and structural identifiability of nonlinear biological systems. Complex. 2019; 2019 https://doi.org/10.1155/2019/8497093

17. Phan T, Bennett J, and Patten T. Practical Understanding of Cancer Model Identifiability in Clinical Applications. Life 2023; 13:410 https://doi.org/10.3390/life13020410 PMID: 36836767

18. Koh T. On the a priori identifiability of the two-compartment distributed parameter model from residual tracer data acquired by dynamic contrast-enhanced imaging. IEEE Trans Biomed Eng. 2007; 55:340–4 https://doi.org/10.1109/TBME.2007.910682

19. Aerts H, Van Riel N, and Backes W. System identification theory in pharmacokinetic modeling of dynamic contrast-enhanced MRI: influence of contrast injection. Magn Reson Med. 2008; 59:1111–9 https://doi.org/10.1002/mrm.21575 PMID: 18429040

20. Brix G, Zwick S, Kiessling F, and Griebel J. Pharmacokinetic analysis of tissue microcirculation using nested models: multimodel inference and parameter identifiability. Med Phys. 2009; 36:2923–33 https://doi.org/10.1118/1.3147145 PMID: 19673191

21. Lopata, R and Riel, N van. Identifiability analysis of the standard pharmacokinetic models in DCE MR imaging of tumours. The 26th Annual International Conference of the IEEE Engineering in Medicine and Biology Society. Vol. 1. IEEE. 2004:1040–3.

22. Lopata RG, Backes WH, van Den Bosch PP, and van Riel NA. On the identifiability of pharmacokinetic parameters in dynamic contrast-enhanced imaging. Magn Reson Med. 2007; 58:425–9 https://doi.org/10.1002/mrm.21336 PMID: 17654583

23. Brix G, Salehi Ravesh M, and Griebel J. Two-compartment modeling of tissue microcirculation revisited. Med Phys. 2017; 44:1809–22 https://doi.org/10.1002/mp.12196 PMID: 28273359

24. Yankeelov TE, and Gore JC. Dynamic contrast enhanced magnetic resonance imaging in oncology: theory, data acquisition, analysis, and examples. Curr. Med. Imaging 2007; 3:91–107 https://doi.org/10.2174/157340507780619179

25. Parker GJ, Roberts C, Macdonald A, Buonaccorsi GA, Cheung S, Buckley DL, et al. Experimentally-derived functional form for a population-averaged high-temporal-resolution arterial input function for dynamic contrast-enhanced MRI. Magn Reson Med. 2006; 56:993–1000 https://doi.org/10.1002/mrm.21066 PMID: 17036301

26. Van Osch MJ, Vonken EjP, Viergever MA, van der Grond J, and Bakker CJ. Measuring the arterial input function with gradient echo sequences. Magn Reson Med. 2003; 49:1067–76 https://doi.org/10.1002/mrm.10461 PMID: 12768585

27. Patlak CS, Blasberg RG, and Fenstermacher JD. Graphical evaluation of blood-to-brain transfer constants from multiple-time uptake data. J Cereb Blood Flow Metab. 1983; 3:1–7 https://doi.org/10.1038/jcbfm.1983.1 PMID: 6822610

28. Tofts PS, and Kermode AG. Measurement of the blood-brain barrier permeability and leakage space using dynamic MR imaging. 1. Fundamental concepts. Magn Reson Med. 1991; 17:357–67 https://doi.org/10.1002/mrm.1910170208 PMID: 2062210

29. Tofts PS, Brix G, Buckley DL, Evelhoch JL, Henderson E, Knopp MV, et al. Estimating kinetic parameters from dynamic contrast-enhanced T1-weighted MRI of a diffusable tracer: standardized quantities and symbols. Magn Reson Med. 1999; 10:223–32

30. Tofts PS. Modeling tracer kinetics in dynamic Gd-DTPA MR imaging. J Magn Reson Imaging 1997; 7:91–101 https://doi.org/10.1002/jmri.1880070113 PMID: 9039598

31. Sahoo P, Rathore RK, Awasthi R, Roy B, Verma S, Rathore D, et al. Subcompartmentalization of extra-cellular extravascular space (EES) into permeability and leaky space with local arterial input function (AIF) results in improved discrimination between high-and low-grade glioma using dynamic contrast-enhanced (DCE) MRI. J Magn Reson Imaging 2013; 38:677–88 https://doi.org/10.1002/jmri.24021 PMID: 23390002

32. Sourbron S, and Buckley DL. Tracer kinetic modelling in MRI: estimating perfusion and capillary permeability. Phys Med Biol. 2011; 57:R1 https://doi.org/10.1088/0031-9155/57/2/R1 PMID: 22173205

33. Yankeelov, TE, Karczmar, GS, and Abramson, RG. Data from QIN-BREAST-02[Dataset]. The Cancer Imaging Archive.

34. Clark K, Vendt B, Smith K, Freymann J, Kirby J, Koppel P, et al. The Cancer Imaging Archive (TCIA): maintaining and operating a public information repository. J Digit Imaging 2013; 26:1045–57 https://doi.org/10.1007/s10278-013-9622-7 PMID: 23884657

35. Barnes SL, Whisenant JG, Loveless ME, Ayers GD, and Yankeelov TE. Assessing the reproducibility of dynamic contrast enhanced magnetic resonance imaging in a murine model of breast cancer. Magn Reson Med. 2013; 69:1721–34 https://doi.org/10.1002/mrm.24422 PMID: 22847762

36. Alliance, Quantitative Imaging Biomarkers. QIBA profile: DCE-MRI quantification (DCEMRI-Q). (2020)

37. Wieland FG, Hauber AL, Rosenblatt M, Tönsing C, and Timmer J. On structural and practical identifiability. Curr Opin Syst Biol. 2021; 25:60–9 https://doi.org/10.1016/j.coisb.2021.03.005

38. Bellman R, and Aström KJ. On structural identifiability. Math Biosci. 1970; 7:329–39 https://doi.org/10.1016/0025-5564(70)90132-X

39. Pohjanpalo H. System identifiability based on the power series expansion of the solution. Math Biosci. 1978; 41:21–33 https://doi.org/10.1016/0025-5564(78)90063-9

40. Karlsson J, Anguelova M, and Jirstrand M. An efficient method for structural identifiability analysis of large dynamic systems. IFAC proceedings volumes 2012; 45:941–6 https://doi.org/10.3182/20120711-3-BE-2027.00381

41. Sedoglavic, A. A probabilistic algorithm to test local algebraic observability in polynomial time. Proceedings of the 2001 international symposium on Symbolic and algebraic computation. 2001:309–17.

42. Ljung L, and Glad T. On global identifiability for arbitrary model parametrizations. Automatica 1994; 30:265–76 https://doi.org/10.1016/0005-1098(94)90029-9

43. Bellu G, Saccomani MP, Audoly S, and D'Angiò L. DAISY: A new software tool to test global identifiability of biological and physiological systems. Comput Methods Programs Biomed. 2007; 88:52–61 https://doi.org/10.1016/j.cmpb.2007.07.002 PMID: 17707944

44. Dong R, Goodbrake C, Harrington HA, and Pogudin G. Differential elimination for dynamical models via projections with applications to structural identifiability. SIAM J Appl Algebra Geom. 2023; 7:194–235 https://doi.org/10.1137/22M1469067

45. Bates DJ, Hauenstein JD, and Meshkat N. Identifiability and numerical algebraic geometry. Plos One 2019; 14:e0226299 https://doi.org/10.1371/journal.pone.0226299 PMID: 31834904

46. Chis OT, Banga JR, and Balsa-Canto E. Structural identifiability of systems biology models: a critical comparison of methods. PloS One 2011; 6:e27755 https://doi.org/10.1371/journal.pone.0027755 PMID: 22132135

47. Raue A, Karlsson J, Saccomani MP, Jirstrand M, and Timmer J. Comparison of approaches for parameter identifiability analysis of biological systems. Bioinform. 2014; 30:1440–8 https://doi.org/10.1093/bioinformatics/btu006 PMID: 24463185

48. Raue A, Kreutz C, Maiwald T, Bachmann J, Schilling M, Klingmüller U, et al. Structural and practical identifiability analysis of partially observed dynamical models by exploiting the profile likelihood. Bioinform. 2009; 25:1923–9 https://doi.org/10.1093/bioinformatics/btp358 PMID: 19505944

49. Murphy SA, and Van der Vaart AW. On profile likelihood. J Am Stat Assoc. 2000; 95:449–65 https://doi.org/10.2307/2669392

50. Murphy RJ, Maclaren OJ, and Simpson MJ. Implementing measurement error models with mechanistic mathematical models in a likelihood-based framework for estimation, identifiability analysis and prediction in the life sciences. J R Soc Interface 2024; 21:20230402 https://doi.org/10.1098/rsif.2023.0402 PMID: 38290560

51. Ochoa-Fernandez R, Abel NB, Wieland FG, Schlegel J, Koch LA, Miller JB, et al. Optogenetic control of gene expression in plants in the presence of ambient white light. Nat. Methods 2020; 17:717–25 https://doi.org/10.1038/s41592-020-0868-y PMID: 32601426

52. Schneider N, Wieland FG, Kong D, Fischer AA, Hörner M, Timmer J, et al. Liquid-liquid phase separation of light-inducible transcription factors increases transcription activation in mammalian cells and mice. Sci Adv. 2021; 7:eabd3568 https://doi.org/10.1126/sciadv.abd3568 PMID: 33523844

53. Simpson MJ, and Maclaren OJ. Profile-Wise Analysis: A profile likelihood-based workflow for identifiability analysis, estimation, and prediction with mechanistic mathematical models. PLoS Comput Biol. 2023; 19:e1011515 https://doi.org/10.1371/journal.pcbi.1011515 PMID: 37773942

54. Simpson MJ, Baker RE, Vittadello ST, and Maclaren OJ. Practical parameter identifiability for spatio-temporal models of cell invasion. J R Soc Interface 2020; 17:20200055 https://doi.org/10.1098/rsif.2020.0055 PMID: 32126193

55. Ebbesen, S, Kiwitz, P, and Guzzella, L. A generic particle swarm optimization Matlab function. American control conference (ACC). IEEE. 2012:1519–24.

56. Kennedy, J, and Eberhart, R. Particle swarm optimization. Proceedings of ICNN'95-international conference on neural networks. Vol. 4. IEEE. 1995:1942–8.

57. Collins DJ, and Padhani AR. Dynamic magnetic resonance imaging of tumor perfusion. IEEE Eng Med Biol. 2004; 23:65–83 https://doi.org/10.1109/MEMB.2004.1360410 PMID: 15565801

58. Woodall RT, Sahoo P, Cui Y, Chen BT, Shiroishi MS, Lavini C, et al. Repeatability of tumor perfusion kinetics from dynamic contrast-enhanced –MRI in glioblastoma. Neurooncol. Adv 2021; 3:vdab174 https://doi.org/10.1093/noajnl/vdab174 PMID: 34988454

59. Choi HS, Kim AH, Ahn SS, Shin Ny, Kim J, and Lee SK. Glioma grading capability: comparisons among parameters from dynamic contrast-enhanced MRI and ADC value on DWI. Korean J Radiol. 2013; 14:487–92 https://doi.org/10.3348/kjr.2013.14.3.487 PMID: 23690718

60. Li X, Zhu Y, Kang H, Zhang Y, Liang H, Wang S, et al. Glioma grading by microvascular permeability parameters derived from dynamic contrast-enhanced MRI and intratumoral susceptibility signal on susceptibility weighted imaging. Cancer Imaging 2015; 15:1–9 https://doi.org/10.1186/s40644-015-0039-z PMID: 25889239

61. Santarosa C, Castellano A, Conte GM, Cadioli M, Iadanza A, Terreni MR, et al. Dynamic contrast-enhanced and dynamic susceptibility contrast perfusion MR imaging for glioma grading: preliminary comparison of vessel compartment and permeability parameters using hotspot and histogram analysis. Eur J Radiol. 2016; 85:1147–56 https://doi.org/10.1016/j.ejrad.2016.03.020 PMID: 27161065

62. Zhao J, Yang Zy, Luo B, Yang J, and Chu J. Quantitative evaluation of diffusion and dynamic contrast-enhanced MR in tumor parenchyma and peritumoral area for distinction of brain tumors. PLoS One 2015; 10:e0138573 https://doi.org/10.1371/journal.pone.0138573 PMID: 26384329

63. Jung SC, Yeom J, Kim JH, Ryoo I, Kim S, Shin H, et al. Glioma: application of histogram analysis of pharmacokinetic parameters from T1-weighted dynamic contrast-enhanced MR imaging to tumor grading. AJNR Am. J. Neuroradiol. 2014; 35:1103–10 https://doi.org/10.3174/ajnr.A3825 PMID: 24384119

64. Nguyen T, Cron G, Perdrizet K, Bezzina K, Torres C, Chakraborty S, et al. Comparison of the diagnostic accuracy of DSC-and dynamic contrast-enhanced MRI in the preoperative grading of astrocytomas. AJNR Am. J. Neuroradiol. 2015; 36:2017–22 https://doi.org/10.3174/ajnr.A4398 PMID: 26228886

65. Arevalo-Perez J, Thomas A, Kaley T, Lyo J, Peck K, Holodny A, et al. T1-weighted dynamic contrast-enhanced MRI as a noninvasive biomarker of epidermal growth factor receptor vIII status. AJNR Am. J. Neuroradiol. 2015; 36:2256–61 https://doi.org/10.3174/ajnr.A4484 PMID: 26338913

66. Ahn SS, Shin NY, Chang JH, Kim SH, Kim EH, Kim DW, et al. Prediction of methylguanine methyltransferase promoter methylation in glioblastoma using dynamic contrast-enhanced magnetic resonance and diffusion tensor imaging. Journal of neurosurgery 2014; 121:367–73 https://doi.org/10.3171/2014.5.JNS132279 PMID: 24949678

67. Wang X, Cao M, Chen H, Ge J, Suo S, and Zhou Y. Simplified perfusion fraction from diffusion-weighted imaging in preoperative prediction of mutation in WHO grade II–III gliomas: comparison with dynamic contrast-enhanced and intravoxel incoherent motion MRI. Radiology and Oncology 2020; 54:301–10 https://doi.org/10.2478/raon-2020-0037 PMID: 32559177

68. Suh C, Kim H, Choi Y, Kim N, and Kim S. Prediction of pseudoprogression in patients with glioblastomas using the initial and final area under the curves ratio derived from dynamic contrast-enhanced T1-weighted perfusion MR imaging. AJNR Am. J. Neuroradiol. 2013; 34:2278–86 https://doi.org/10.3174/ajnr.A3634 PMID: 23828115

69. Yun TJ, Park CK, Kim TM, Lee SH, Kim JH, Sohn CH, et al. Glioblastoma treated with concurrent radiation therapy and temozolomide chemotherapy: differentiation of true progression from pseudoprogression with quantitative dynamic contrast-enhanced MR imaging. Radiology 2015; 274:830–40 https://doi.org/10.1148/radiol.14132632 PMID: 25333475

70. Hylton N. Dynamic contrast-enhanced magnetic resonance imaging as an imaging biomarker. J Clin Oncol 2006; 24:3293–8 https://doi.org/10.1200/JCO.2006.06.8080 PMID: 16829653

71. Kickingereder P, Wiestler B, Graf M, Heiland S, Schlemmer HP, Wick W, et al. Evaluation of dynamic contrast-enhanced MRI derived microvascular permeability in recurrent glioblastoma treated with bevacizumab. J Neurooncol. 2015; 121:373–80 https://doi.org/10.1007/s11060-014-1644-6 PMID: 25359396

72. Xiao J, Rahbar H, Hippe DS, Rendi MH, Parker EU, Shekar N, et al. Dynamic contrast-enhanced breast MRI features correlate with invasive breast cancer angiogenesis. NPJ Breast Cancer 2021; 7:42 https://doi.org/10.1038/s41523-021-00247-3 PMID: 33863924

73. Minosse S, Picchi E, Ferrazzoli V, Pucci N, Da Ros V, Giocondo R, et al. Influence of scan duration on dynamic contrast-enhanced magnetic resonance imaging pharmacokinetic parameters for brain lesions. Magn. Reson. Imaging 2024; 105:46–56 https://doi.org/10.1016/j.mri.2023.11.002 PMID: 37939968

74. Joint Head and Neck Radiotherapy-MRI Development Cooperative. A multi-institutional comparison of dynamic contrast-enhanced magnetic resonance imaging parameter calculations. Sci Rep. 2017; 7:11185 https://doi.org/10.1038/s41598-017-11554-w PMID: 28894197

75. QIBA MR Biomarker Committee. MR DCE Quantification. Quantitative Imaging Biomarkers Alliance. Profile Stage: Public Comment. December 10, 2020. Available from: https://qibawiki.rsna.org/index.php/Profiles

76. Sanvito F, Raymond C, Cho NS, Yao J, Hagiwara A, Orpilla J, et al. Simultaneous quantification of perfusion, permeability, and leakage effects in brain gliomas using dynamic spin-and-gradient-echo echo-planar imaging MRI. Eur Radiol. 2023:1–15 https://doi.org/10.1007/s00330-023-10215-z PMID: 37882836